Three-Dimensional Turbulent Boundary-Layer Development on a Fan Rotor Blade

B. Lakshminarayana,* C. Hah,† and T. R. Govindan‡
The Pennsylvania State University, University Park, Pennsylvania

This paper is concerned with an experimental study undertaken to measure the boundary-layer growth on a fan rotor blade. The measurements were carried out at various chordwise and radial locations on both surfaces of the blade using a miniature "X" configuration hot-wire probe. The streamwise and radial velocity profiles are interpreted and correlated. The validity of conventional velocity profiles, such as the "law of the wall" for the streamwise profile and the hodograph plot for the cross-flow profile are examined. The measured values of boundary-layer growth properties are compared with the predictions based on a momentum-integral technique.

Nomenclature

C	= chord length
C_p	= pressure coefficient $= 2(p_\ell - p_1)/\rho U_1^2$
H	$= \delta_1/\theta_{11}$
i	= incidence angle
p_ℓ	= local blade static pressure
PR, SU	= pressure and suction surfaces, respectively
R	$= r/r_{tip}$
S	$= s/C$
s,n,r	= streamwise, normal, and radial directions (orthogonal to each other) shown in Fig. 1; $s=0$ at the leading edge, $n=0$ on the blade surface, $r=0$ at the axis
t	= blade spacing
U	= streamwise (s) relative velocity normalized by U_e (Fig. 1)
U_e	= local freestream (or edge) relative velocity (Fig. 1)
U_1, p_1	= inlet relative velocity and static pressure
W	= radial velocity normalized by U_e (Fig. 1)
$\theta_{11}, \theta_{12}, \theta_{22}$, δ_1, δ_2, H	= defined in Eq. (2)
ζ	= loss coefficient [Eq. (3)]
θ_c	= camber angle
δ	= boundary-layer thickness
ν	= kinematic viscosity
ϵ	= tangent of the limiting streamline angle (angle of the streamline as the blade surface is approached)
λ	= stagger angle
β_1, β_2	= inlet and exit relative flow angle

Introduction

A KNOWLEDGE of the characteristics of the three-dimensional boundary layer on rotor blades is essential for the analysis and design of these machinery as well as for the prediction of flow properties, losses, and noise generated in them. The Coriolis and centrifugal forces generate spanwise flows inside the blade boundary layers, the magnitude of which depends upon the angular velocity of the rotor, the flow coefficient, and the rotor-blade geometry. In addition, near the tip and hub of the rotor, complex flow interactions take place between the blade boundary layer and the end wall flows. Because of the complicated nature of the problem, compressor, turbine, and fan rotor blade boundary layers continue to the one of the least understood phenomena in turbomachinery, and very few investigators have attempted measurements or analysis of these flows.

The earlier experimental investigations related to the rotor blade boundary layer were confined to an axial-flow inducer passage and were carried out by the Penn State group.[1-4] These investigations were carried out using a single helical blade,[1] and a flat plate helical channel.[2-4] All of these investigations were carried out at low flow coefficients with very mild chordwise and radial pressure gradients. The rotors employed consisted of zero-cambered blades of large chord length. Hence, there was felt a need to extend such investigations to a compressor type of blading, where three-dimensional effects due to curvature and rotation, in combination with the pressure gradients, are likely to have a substantial influence on the boundary layer development. This prompted the present investigation. The boundary layer on a low-speed fan rotor blade was measured at several chordwise and radial locations, using a miniature "X" configuration hot-wire probe. The data are compared with the predictions from the momentum-integral analysis.[5]

Facility, Measurement Technique, and Program

Measurements reported in this paper were carried out using the Axial Flow Fan Research Facility (AFRF) at the Applied Research Laboratory. The facility and the rotor are described in detail in Ref. 6. A brief description follows.

A nine-bladed rotor with cambered blades (British Cl Profile) was installed in the facility and had the following specifications: tip diameter = 0.54 m, hub/tip diameter ratio = 0.44, blade chord (const) = 15.24 cm, maximum thickness (const) = 1.5 cm. Blade spacing, stagger angle, and incidence angle at midradius were 13.72 cm, 50 deg and 2.94 deg, respectively. Other relevant data are tabulated in Table 1. The blade was designed for the free vortex distribution with substantial radial twist in the blade geometry. The performance, as well as wake characteristics, of this rotor are given in Refs. 7 and 8. The rotor alone (no IGV or stator) was operated at the design condition, 1150 rpm. The design flow coefficient of 0.6 was achieved by means of an auxiliary fan at the exit of the facility. The axial velocity at inlet was 13.6 m/s.

Presented as Paper 82-1007 at the AIAA/ASME Third Joint Thermophysics, Fluid, Plasma, and Heat Transfer Conference, St. Louis, Mo., June 7-11, 1982; submitted June 17, 1982; revision received March 17, 1983. This paper is declared a work of the U.S. Government and therefore is in the public domain.

*Director of Computational Fluid Dynamics Studies and Professor of Aerospace Engineering, Dept. of Aerospace Engineering. Fellow AIAA.

†Research Associate, Dept. of Aerospace Engineering. Member AIAA.

‡Graduate Assistant, Dept. of Aerospace Engineering. Member AIAA.

The Reynolds number based on the inlet relative velocity and chord length at midspan was 2.8×10^5.

All of the measurements were taken with a hot-wire probe rotating with the rotor. This is accomplished by driving an internal probe traverse assembly with a stepping motor and a gear reduction unit that permits increments of 0.083 deg, which facilitates measurement at 482 locations in each blade passage. Details of this rotating probe traverse assembly are given in Ref. 6.

A miniature cross-flow X hot-wire probe, TSI 1247, with sensor diameter of 3 μm and sensor length equal to 1 mm was used in this program. Both the sensors are within a circle of approximate diameter 1.5 mm. The sensors were located in the (sr) plane with their axis at 45 deg to the s axis (Fig. 1) and were traversed normal to the blade surface. The mean and the rms value of the fluctuating voltages from each of these wires were transmitted through a slip-ring unit and noted. Since the flow traverse was done close to the blade surface, the component of velocity in the n direction (V) is assumed to be small. The present configuration and the relevant hot-wire equations will provide the values of the streamwise velocity U, radial velocity W, and the resultant turbulence intensity in the (sr) plane, T_{sr}. Corrections were made for the deviation from the cosine law. The heat-transfer characteristics of the hot-wire sensor are altered close to the wall. The error in the hot-wire data due to the wall vicinity effect was corrected by calibrating the probe as a function of the distance of the probe from the wall and by measuring the mean voltages (E_0) at zero velocity with the probe near the blade surface.

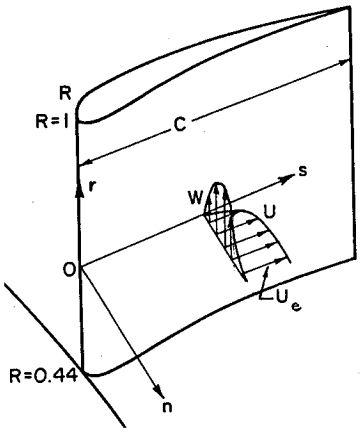

Fig. 1 Nature of blade boundary layer and notations used.

Table 1 Rotor blade characteristics (design)

R	C/t	λ, deg	θ_c, deg	β_1 deg	β_2 deg	i, deg
0.44	1.81	23.14	35.64	45.66	13.21	4.70
0.50	1.61	31.02	28.12	49.06	24.35	3.98
0.61	1.31	42.44	17.87	54.68	40.01	3.30
0.72	1.11	50.28	11.74	57.08	47.87	2.94
0.83	0.96	55.78	8.01	63.59	58.48	2.80
0.94	0.85	59.85	5.71	65.43	61.18	2.72
1.0	0.80	61.59	4.80	66.56	63.06	2.66

The boundary-layer measurement was carried out at $R = 0.54$, 0.72, 0.86, and 0.94, and at various chordwise and radial locations as shown in Table 2. All of the data, except those at $R = 0.86$, are presented and interpreted in this paper.

Experimental Results and Interpretation

The radial variation of axial velocity and the absolute tangential velocity at the inlet and exit of the blade row are presented in Ref. 8. These plots indicate that the locations $R = 0.54$ and 0.94, where the blade boundary layers were measured, are in the outer layer of hub wall and annulus wall boundary layers, respectively.

The blade pressure distributions at three typical radii, one each near the hub, midradius, and the tip measured by Pierzga[6] are shown in Fig. 2. The blade pressure distributions derived from the computer program for the meridional and the blade-to-blade solutions developed by Katsanis and McNally[9] and Katsanis,[10] respectively, are also shown in Fig. 2. Steep chordwise pressure gradient near the suction surface is clearly evident from the data shown. This should have substantial influence on the boundary-layer growth on the suction side. The agreement between the predicted and the measured values is good, except near the leading edge of the pressure surface. The predictions are not satisfactory at $R = 0.853$. This region is influenced by the wall and viscous effects. The theoretical pressure distribution is used in the prediction of the boundary-layer growth described later.

The boundary-layer data at $R = 0.54$, 0.72, and 0.94, and at various chordwise locations on both surfaces of the blade will be presented in the following sections. The notations used are shown in Fig. 1 and defined in the nomenclature. All

Table 2 Values of θ_{11}, δ_1, H, U_e and ϵ (predicted) at various radial and chordwise positions

Radius	Chordwise station, S	U_e, m/s	$\delta_1 \times 10^3$	$\delta_2 \times 10^3$	$\theta_{11} \times 10^3$	$\theta_{12} \times 10^3$	$\theta_{22} \times 10^6$	H	ϵ predicted
0.54	0.20	18.8	0.69	−0.089	0.34	−0.006	−0.230	2.048	0.05
Pressure	0.72	17.4	1.96	−0.766	1.22	−0.150	−10.820	1.602	0.25
	1.00	18.0	1.25	0.284	0.85	−0.017	−0.392	1.465	0.37
0.54	0.32	21.8	2.86	1.447	2.18	0.186	−8.505	1.308	0.08
Suction	0.41	16.7	7.47	3.168	5.80	0.414	−0.070	1.288	0.12
	1.00	14.4	2.17	6.868	1.76	0.221	−9.436	1.234	0.49
0.72	0.16	22.7	0.83	−0.120	0.44	−0.012	−0.536	1.897	0.03
Pressure	0.69	21.1	2.61	−1.333	1.73	−0.304	−20.840	1.509	0.29
	1.00	21.3	2.49	−0.091	1.85	−0.011	−0.102	1.343	0.37
0.72	0.36	24.3	1.11	0.264	0.71	0.002	−0.609	1.560	0.12
Suction	0.74	22.6	7.56	4.209	5.31	1.035	−31.670	1.422	0.15
	1.00	18.0	9.03	6.422	7.15	1.173	−24.130	1.263	0.50
0.86	0.38	28.1	2.18	−0.992	1.56	0.132	−6.014	1.398	0.14
Suction	0.79	23.8	3.49	1.915	2.63	0.293	−11.580	1.330	0.39
0.94	0.12	25.3	0.89	0.194	0.53	0.011	−0.335	1.669	—
Pressure	0.55	24.1	0.60	0.0196	0.26	0.000	−0.028	2.262	—
	1.00	22.7	3.33	0.406	2.67	0.049	−0.577	1.245	—
0.94	0.50	28.6	1.86	−0.544	1.31	−0.063	−1.835	1.418	—
Suction	1.00	23.8	1.10	−0.021	0.73	0.002	−0.037	1.507	—

velocities are normalized by the local freestream-relative velocity (e.g., U is the nondimensionalized streamwise velocity, W the nondimensionalized radial velocity). S is the chordwise distance s normalized by local blade chord, and N the distance n normal to the blade nondimensionalized by the blade spacing.

Streamwise Component of Velocity Profile (U)

The streamwise velocity U is the resultant component of relative velocity lying on the cylindrical surface at a particular radius (Fig. 1). The distribution of the streamwise velocity profile on both surfaces of the blade at various chordwise locations at $R=0.54$, 0.72, 0.94, is shown plotted in Figs. 3, 4, and 5, respectively.

The profile on the suction side at $R=0.54$ indicates the expected adverse pressure gradient effect. One possible reason for the sudden decrease in the boundary-layer growth (Fig. 3) from midchord to the trailing edge is the presence of the radial outward transport caused by rotation and secondary flow. The data at $R=0.72$ and $S=1.00$ (Fig. 4), where a sudden increase in the boundary-layer growth and a change in the velocity profile is observed near the trailing edge, seem to indicate the validity of such a hypothesis. The boundary-layer thickness varies from a maximum of 5% of blade spacing near the suction surface to 2% near the pressure surface.

The boundary-layer data derived from the measurements at $R=0.72$, reported in this paper, and the wake profiles derived from the measurements of Ref. 7, are shown in Fig. 4. The boundary-layer growth on the suction side is substantially higher than other radii. The profile undergoes a drastic change from $S=0.74$ to 1.0 in this region. The nature of the profile seems to indicate the presence of substantial three-dimensional effects caused by the outward boundary-layer movement in the trailing edge region. This is in conformity with the observations of Dring et al.,[11] based on the flow visualization experiments. The data on the pressure side at $R=0.72$ also show a change in the velocity profile and a decrease in velocity defect near the blade surface as the flow approaches the trailing edge. The boundary-layer growth is rapid on both the surfaces near the trailing edge. The boundary-layer thickness varies from a maximum 6% of blade spacing near the suction side to 4% near the pressure side. The wake data, shown in Fig. 4, indicate relatively small diffusion on the suction side, but a large spreading rate on the pressure side.

The data at $R=0.94$ (Fig. 5), suction side, indicate an unusual trend. The velocity defect at $S=0.50$ near the blade surface is substantially reduced as the flow approaches the trailing edge. This is probably caused by the radial outward transport inside the blade boundary layers discussed earlier. But the trend on the pressure side indicates a substantial growth in the boundary layer near the trailing edge. This may have been caused by relatively small radial velocities (discussed later) observed on the pressure side at all radii and the presence of a scraping vortex.

Power Law Profiles

Figure 6 shows a comparison between a typical set of the measured streamwise velocity profiles and those derived by using the power law profile,

$$U=(n/\delta)^{(H-1)/2} \tag{1}$$

To derive these profiles, the shape factor H and the displacement thickness δ_1 of the measured profiles were used (Table 2). The boundary-layer thickness, δ, was computed from the shape factor, the displacement thickness, and the form of the power law profile. The comparisons range from very good to poor and are related to the location, shape

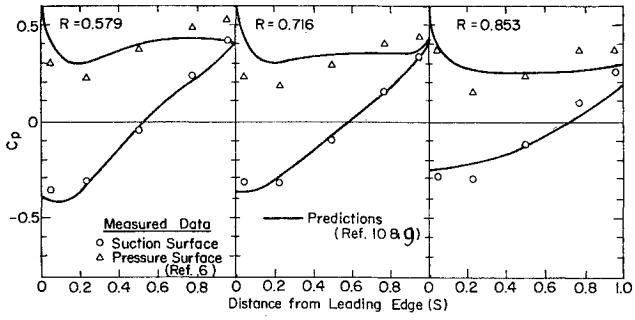

Fig. 2 Measured[6] and predicted blade pressure distribution.

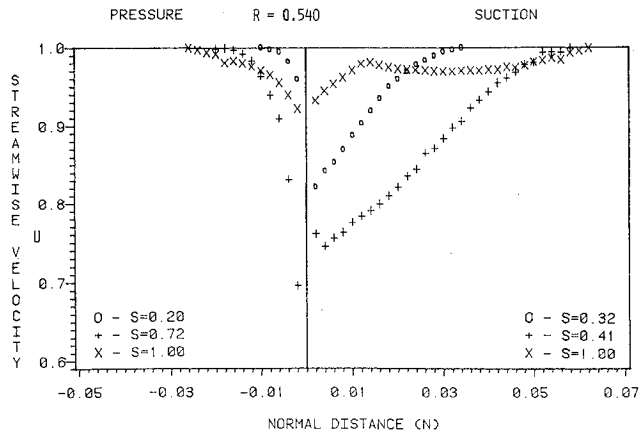

Fig. 3 Streamwise velocity (U) profile, $R=0.54$.

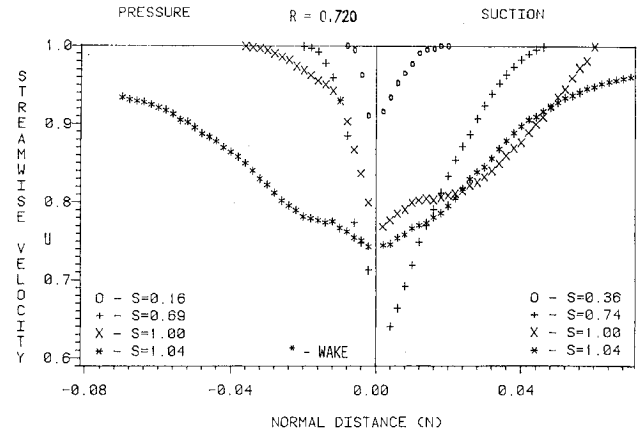

Fig. 4 Streamwise velocity (U) profile, $R=0.72$.

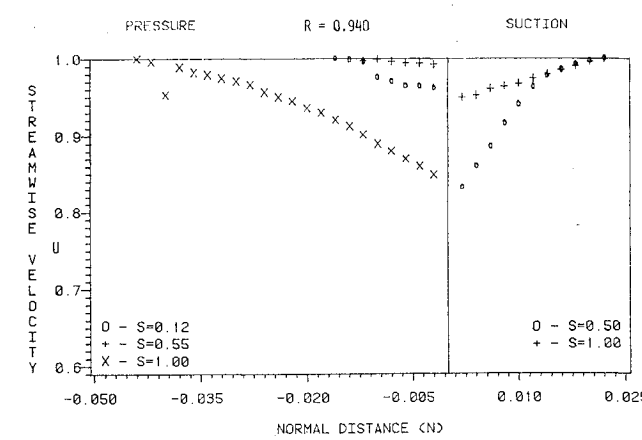

Fig. 5 Streamwise velocity (U) profile, $R=0.94$.

factor, and thickness of the boundary layer. The comparison is very good for the curve labeled 5 at midradius, on the suction side, which has a shape factor of 1.42. This is in the shape factor range typical for many turbulent boundary layers. The comparison deteriorates for shape factors below and above this value, for thinner boundary-layer thicknesses, and as we move away from the midradius locations. The comparisons are moderately good for curves 2 and 4 with shape factors 1.29 and 1.34, respectively. The thicker boundary layer at $R=0.54$ and $S=0.41$ (SU) is better represented than the thinner layer at $R=0.72$, $S=1.0$ (PR). The thin boundary layer at $R=0.54$, $S=0.72$ (PR) and $R=0.72$, $S=0.69$ (PR), are not very well represented by the power law profile. The inner part of the layer is well represented but is poor at the edge of the layer. These two measurements represent larger values of the shape factor, being 1.60 for the first case (curve 1) and 1.51 for the second case (curve 3). The representation is poor for measurements close to the tip of the blade ($R=0.94$, curves 6, 7, and 8 in Fig. 6). The representation does improve as the thickness of the boundary layer increases (curve 8).

Logarithmic Plot of Velocity Profile

Figure 7 shows a plot of the streamwise velocity, normalized by the edge velocity (U_e) vs the Reynolds number based on the edge velocity and the distance normal to the wall, plotted on a semilog graph. If the friction velocity were used instead of the edge velocity, the data would collapse to a single curve given by the "law of the wall" and the "law of the wake" equations. However, reliable estimates of the friction velocity could not be obtained in this case by the extrapolation of the available data to the blade surface. This is due to the scatter in the data near the blade surface. However, the plots in Fig. 7 do show a linear region in the inner part of the profile indicating a logarithmic region in the velocity profile near the blade surface. The data depart from this linear region, on the semilog plot, in the outer layer. The departure is most dramatic on the suction side due to the adverse pressure gradient and reveals the presence of a large wake region in the suction surface boundary layer.

Radial Velocity Profile (W)

The radial velocity profiles at $R=0.54$, 0.72, and 0.94, and at various chordwise locations are shown plotted in Figs. 8, 9, and 10, respectively. The positive values signify radial outward velocities. At $R=0.54$ (Fig. 8), the radial velocities are mostly inward and small on the pressure side, but outward and large on the suction side. The effect of blade rotation and the secondary flow near the hub have a cumulative effect on the suction side resulting in the observed trend. The presence of large radial velocities near the suction side, especially at $S=0.41$ and 1.0, is clear evidence of the additive effect of the rotation and the secondary flow in this region. It is clear that the inward flow due to the secondary flow near the hub on the pressure side is substantially reduced by the rotation, which has a tendency to induce outward flows. The expected trend, namely the location of the maximum radial velocities near the blade surface, occurs only at $S=0.32$ near the suction side. At other locations ($S=1.0$ and 0.41 near the suction surface), the maximum values occur near the center-of-blade boundary layer. This trend indicates the influence of the secondary flow that exists near both surfaces.

The radial velocity profiles at $R=0.72$ are shown in Fig. 9. Even at this radius, the radial velocities are small and inward on the pressure side and large and outward on the suction side. There is no reasonable explanation for the inward flow at the blade trailing edge on the pressure side except for the possible existence of a trailing vortex system which will

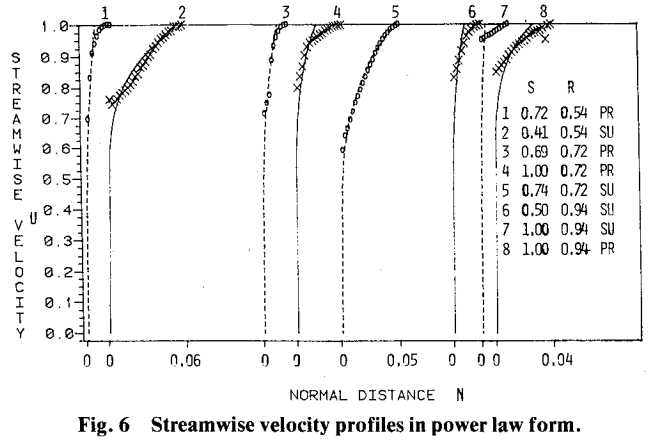

Fig. 6 Streamwise velocity profiles in power law form.

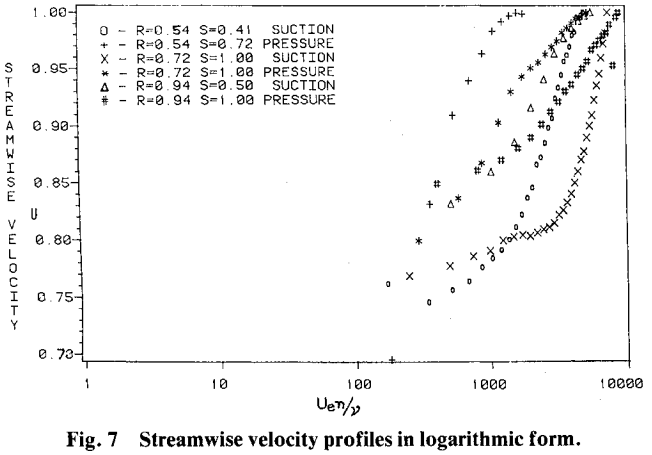

Fig. 7 Streamwise velocity profiles in logarithmic form.

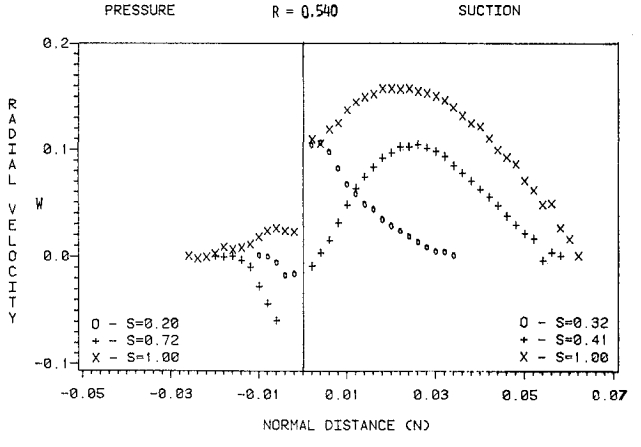

Fig. 8 Radial velocity (W) profiles, $R=0.54$.

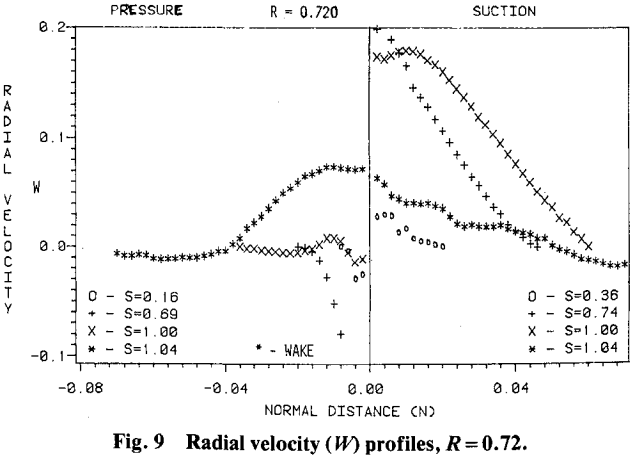

Fig. 9 Radial velocity (W) profiles, $R=0.72$.

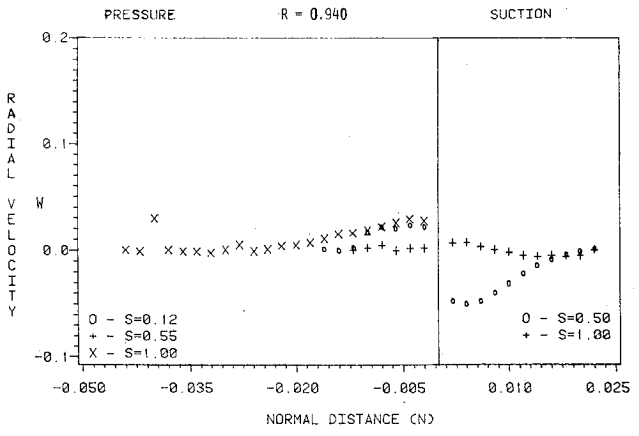

Fig. 10 Radial velocity (W) profiles, $R=0.94$.

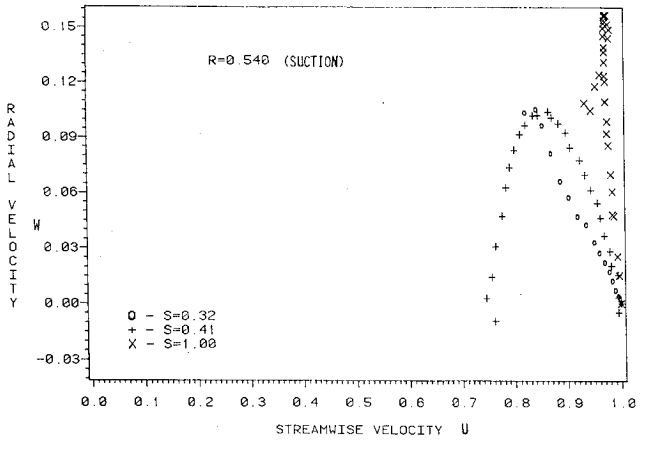

Fig. 11 Hodograph plot of streamwise and radial velocity, $R=0.54$ (SU).

provide inward and outward velocities on either side of the blade. The radial velocities in the wake are outward in this region. The radial velocity profiles near the suction side show the usual trend, namely maximum velocities near the blade surface decreasing to zero in the outer edge of the blade boundary layer. The radial velocity increases continuously from very small values at $S=0.36$ to large values at $S=1.0$ at all locations inside the blade boundary layer. The maximum values are about the same order as those observed at $R=0.54$. Near the trailing edge of the suction side, the radial velocities are found to be large for a substantial portion of the inner region of the blade boundary layer. The existence of near-stall conditions at this location may account for the large radial velocities observed in a substantial portion of the boundary layer.

The radial velocities are found to be small at $R=0.94$ (Fig. 10). The effect of the annulus wall in reducing the radial velocities is clearly evident. The radial velocity in this region is influenced by the leakage flow, annulus-wall boundary layer, and the blade rotation. The leakage flow would induce radial outward velocity near the pressure surface and inward velocity near the suction surface of the blade. The dominant effect of the leakage flow, which has a tendency to induce a radial inward velocity on the suction side (as opposed to outward velocities resulting from the rotation) is clearly evident.

Hodograph Plot

The streamwise and the radial component of velocities are shown plotted in the hodograph from Figs. 11 and 12 for $R=0.54$ and 0.72, respectively. Since the radial velocities are

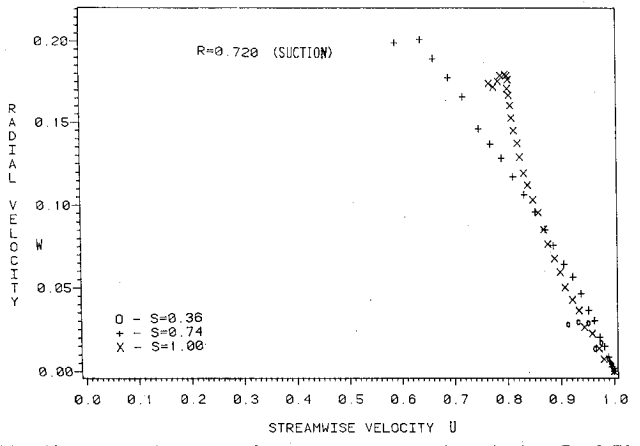

Fig. 12 Hodograph plot of streamwise and radial velocity, $R=0.72$ (SU).

very small on the pressure side of the blade, only the data on the suction side are shown plotted. The data at $R=0.54$ (Fig. 11) show the existence of a linear outer region only for $S=0.32$. The profiles at other clockwise locations are unconventional. The hodograph plot for $R=0.72$, shown in Fig. 12, indicates that the profiles are well behaved, with the existence of nearly linear regions in the outer layer of the boundary layer at all the chordwise locations. It is not certain from the plot whether the collateral region exists near the surface, even though the first data point is at 3-5% of the blade boundary-layer thickness (Fig. 9) from the blade surface. The hodograph plot for $R=0.94$ revealed no systematic behavior, and hence it not shown herein. Since the radial velocities are small and are influenced mainly by the leakage flow at this radius, no systematic trend is expected in this region.

Displacement and Momentum Thicknesses and Shape Factor, and Comparison with Predictions

The momentum and displacement thicknesses, and the shape factor are defined by

$$\theta_{11}=\frac{1}{C}\int_0^h U(1-U)\,dn, \qquad \theta_{12}=\frac{1}{C}\int_0^h W(1-U)\,dn$$

$$\theta_{21}=-\frac{1}{C}\int_0^h UW\,dn, \qquad \theta_{22}=-\frac{1}{C}\int_0^h (W)^2\,dn$$

$$\delta_1=\frac{1}{C}\int_0^h (1-U)\,dn \qquad \delta_2=-\frac{1}{C}\int_0^h W\,dn$$

$$h>\delta \qquad H=\delta_1/\theta_{11} \qquad (2)$$

The values of all the thicknesses derived from the data are shown in Table 2. Caution should be exercised in utilizing the values of θ_{12}, θ_{22}, δ_2 as their magnitudes are small and depend on the accuracy of measurement of radial velocities.

The values of δ_1, θ_{11}, and H derived from the measured data, shown in Figs. 13 and 14, and 15, respectively, are compared with the predictions based on the momentum-integral technique developed by Lakshminarayana and Govindan.[5] The momentum-integral equations were derived by integrating the streamwise and radial momentum equations normal to the surface of the blade. Head's entrainment equation was used to model the variation of the shape factor and close the system of equations. Power law profile [Eq. (1)] for the streamwise velocity and Mager's profile for the radial velocity were used. The pressure distribution impressed on the boundary layer the outer inviscid flow was obtained by the method of Katsanis and McNally[9,10] (Fig. 2).

The predictions of θ_{11}, δ_1, and H are good on the pressure side at midradius and on the suction side at $R=0.86$, where the momentum-integral equations are most applicable. However, the predictions are poor toward the trailing edge on the suction side at $R=0.72$. An examination of the measured velocity profiles near the trailing edge on the suction side at $R=0.54$ and $R=0.72$ (Figs. 3 and 4) show "separated flow"-like profiles. In such regions of the flow, a large radial migration of low momentum fluid toward the tip occurs. The large momentum thickness measured near the trailing edge on the suction side at $R=0.72$ is probably indicative of this process. The momentum-integral equations do not contain these flow processes and are unable to predict them resulting in an underprediction at $R=0.72$ and an overprediction at $R=0.54$, near the trailing edge. Another effect absent in the momentum-integral equations is the effect of the end walls. This effect is only approximately accounted for in the method of Ref. 5 and is probably one of the causes for the poor predictions near the hub walls ($R=0.54$). Another critical factor in the momentum-integral equations is the inviscid pressure distribution that is input into the equations. Inability to input local gradients of the pressure accurately deteriorates the predictions obtained from the method. This is particularly true toward the trailing edge where proper trailing-edge conditions are not imposed in the inviscid code,[5] leading to poor input of the radial pressure gradient in these regions. The shape factor distributions (Fig. 15) are well predicted at most locations. Seemingly, some of the errors described above tend to compensate in the shape factor distribution, being present in both the momentum and displacement thicknesses. The predicted limiting streamline angle (Table 2) is generally overpredicted by the method, particularly near the trailing edge, when compared with the values on the hodograph plots. The prediction of the limiting streamline angle is sensitive to the input radial pressure gradient and is probably the cause of the higher prediction.

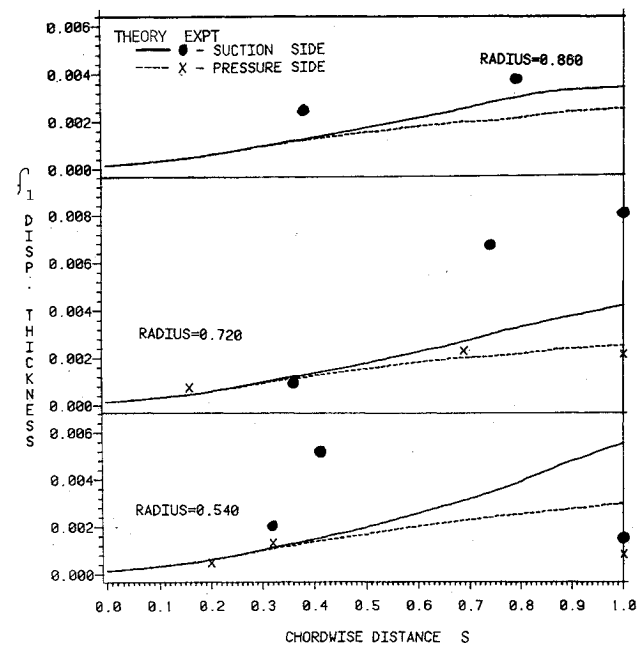

Fig. 13 Chordwise variation of displacement thickness (δ_1).

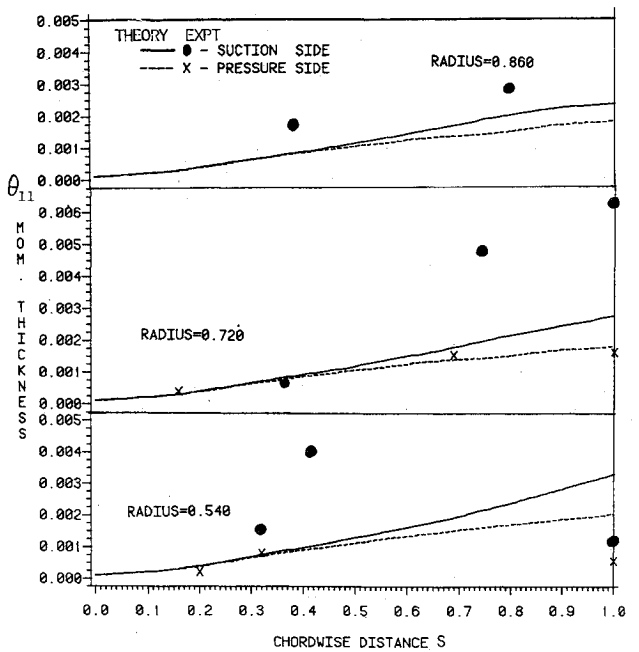

Fig. 14 Chordwise variation of momentum thickness (θ_{11}).

At $R=0.54$, the momentum (θ_{11}) and displacement (δ_1) thicknesses increase up to $S=0.31$ and then decrease slightly as the flow approaches the trailing edge. This is attributed to the radial migration of the boundary layer. At $R=0.72$, the measured θ_{11} and δ_1 distribution indicate that the increase is gradual on the pressure side. There is a dramatic increase (Table 2, Figs. 13 and 14) in the momentum and displacement thickness from $S=0.36$ to 1.0 on the suction side. This is again attributed to migration of the boundary layer from the lower radius.

The profile loss coefficient ζ ($=\Delta P_0/\frac{1}{2}\rho U_1^2$, where ΔP_0 is the stagnation pressured loss) was calculated from the following equation derived by Speidel[12] for the two-dimensional flow. This is an approximation as a corresponding equation for the three-dimensional flow is not available.

$$\zeta = 2C\theta_{11}(\cos^2\beta_1/t\cos^3\beta_2) \tag{3}$$

The predicted values of ζ are based on the design values of β_1 and β_2, and the predicted values of θ_{11} (sum of the values on both surfaces near the trailing edge). This is a logical choice since the input to the inviscid program was based on the design values. The measured values of ζ are derived from the measured values of data for β_1 and β_2, and θ_{11} reported in this paper. The measured value of the loss coefficient is compared with the predicted value in Fig. 16. The agreement

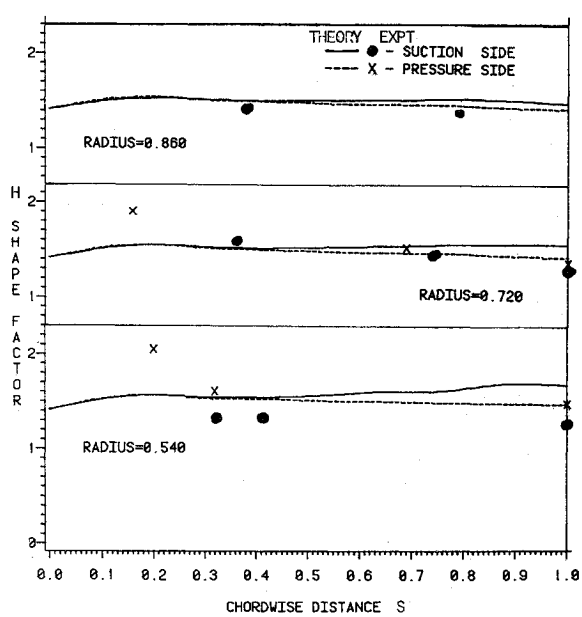

Fig. 15 Chordwise variation of shape factor (H).

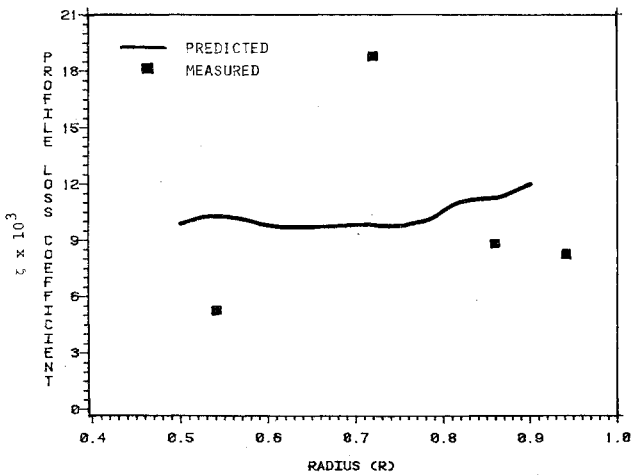

Fig. 16 Measured and predicted values of profile loss coefficient (ζ).

is poor near the hub and midradius and good near the tip. Poor agreement between the prediction and the measurement from hub to midradius may be due to large radial velocities that exist on the suction side, from the hub to midradius, with a consequent increase in the momentum thickness near midradius. The feature may be inherent in the design as a large change in the camber angle occurs between $R=0.50$ and 0.60 (Table 1), resulting in a large radial pressure gradient at these radial locations.

Conclusions

1) The boundary-layer profiles on fan rotor blades are three-dimensional, with appreciable radial velocities on the suction side of the blade.

2) The velocity profiles near the trailing-edge location on the suction side are substantially altered by the radial outward migration of the boundary layer.

3) The streamwise velocity profiles exhibit the presence of the "logarithmic" (law of the wall) and the "wake" regions. The suction side boundary layer have substantial "wake" regions in the outer layer.

4) The radial velocity distribution indicates the influence of the secondary flow in the hub region and the leakage flow in the tip region. The radial component of velocities are high on the suction side near midradius, with peak values occurring close to the blade surface. Small radial inward velocities are observed on the pressure side at midradius.

5) The hodograph plot of the velocity components reveals the presence of a linear region in the otuer layer at midradius. The collateral region near the blade surface is either small or nonexistent.

6) The boundary layers are very thin near the pressure side. The boundary-layer thickness varies from 5-7% of blade spacing on the suction side of the trailing edge.

7) The momentum and displacement thicknesses show a rapid increase from midchord to trailing edge on the suction side at midradius. This is attributed to the radial outward migration of the blade boundary layer from lower radii where a decrease in these thicknesses are observed from midchord to trailing edge.

8) The predictions of the boundary-layer properties (θ_{II}, δ_I) based on the momentum-integral technique is in good agreement with the data on the pressure side at midradius and on the suction side at $R=0.86$. Maximum discrepancies between the two are observed near the trailing edge of the suction surface at $R=0.72$ and 0.54. These are attributed to large radial migration that exists during near-stall conditions.

Acknowledgments

This work was supported by the U.S. National Aeronautics and Space Administration through Grant NsG 3266 with P. M. Sockol as the Technical Monitor. The experimental work was carried out at the Applied Research Laboratory in their Axial Flow Research Fan Facility. Assistance by J. Rishell and G. B. Gurney is gratefully acknowledged.

References

[1] Lakshminarayana, B., Jabbari, A., and Yamoka, H., "Three Dimensional Turbulent Boundary Layer on a Single Rotating Helical Blade," *Journal of Fluid Mechanics*, Vol. 51, 1972, pp. 545-569.

[2] Anand, A. K. and Lakshminarayana, B., "Three Dimenional Turbulent Boundary Layer in a Rotating Helical Channel," *Journal of Fluids Engineering*, Vol. 97, June 1975, pp. 197-210.

[3] Anand, A. K. and Lakshminarayana, B., "An Experimental and Theoretical Investigation of Three Dimensional Turbulent Boundary Layer Inside an Axial Flow Inducer," NASA Contractor Rept. 2888, Aug. 1977.

[4] Anand, A. K. and Lakshminarayana, "Three Dimenisonal Turbulent Boundary Layer in a Rotating Helical Channel," *Journal of Engineering for Power*, Vol. 100, June 1978, pp. 676-690.

[5] Lakshminarayana, B. and Govindan, T. R., "Analysis of Turbulent Boundary Layer on a Cascade and Rotor Blades of Turbomachinery," *AIAA Journal*, Vol. 19, No. 10, 1981, pp. 1333-1341.

[6] Pierzga, M. J., "Experimental Verification of the Streamline Curvature Analysis Method Applied to the Flow Through an Axial Flow Fan," M.S. Thesis, Dept. of Aerospace Engineering, The Pennsylvania State University, 1981; also, ARL TM 80-181, 1980.

[7] Lakshminarayana, B., Govindan, T. R., and Reynolds, B., "Effects of Rotation and Blade Incidence on Properties of Turbomachinery Rotor Wake," *AIAA Journal*, Vol. 20, No. 2, Feb. 1982, pp. 245-253.

[8] Lakshminarayana, B., Govindan, T. R., and Reynolds, B., "Effects of Blade Loading and Rotation on Compressor Rotor Wake in Endwall Regions," *AIAA Journal*, Vol. 21, No. 3, 1983, pp. 407-414.

[9] Katsanis, T., and McNally, W. D., "Revised Fortran Program for Calculating Velocities and Streamlines on the Hub-shroud Mid Channel Stream Surface of an Axial-, Radial, and Mixed-Flow Turbomachine or Annular Duct," NACA TND 8430, 1977.

[10] Katsanis, T., "Use of Arbitrary Quasi-orthognoals for Calculating Flow Distribution on a Blade to Blade Surface in a Turbomachine," NASA TND 2809, 1965.

[11] Dring, R. P., Joslyn, H. D., and Hardin, L. W., "An Investigation of Compressor Rotor Aerodynamics," *Journal of Engineering for Power*, Vol. 104, Jan. 1982, pp. 84-90.

[12] Speidel, L., "Berechnung Der Strömungsverluste von Ungestaffelten Ebenen Schaufelgittern, *Ingenieur Archiv* 22, 1954, pp. 295-322.